Influence of experimental parameters on spatial phase distribution in as-sprayed and incubated hydroxyapatite coatings

**Christoph Hesse · Margitta Hengst ·
Reinhard Kleeberg · Jens Götze**

Abstract In the present study, the behavior and properties of plasma-sprayed hydroxyapatite coatings [$Ca_{10}(PO_4)_6(OH)_2$, HAp] were investigated in relation to the spraying process. The experiments were focused on the influence of type of feedstock and spray power on the phase composition and distribution within the coatings. Depth profiles of the coatings were investigated before and after incubation in revised simulated body fluid (SBF) by X-ray diffraction and infrared spectroscopy. Besides HAp, the coatings contain oxyapatite (OAp) and carbonate apatite (CAp). Additionally, tricalcium phosphate (TCP), tetracalcium phosphate (TTCP), CaO, and an amorphous phase were detected in the coatings. The HAp content directly depends on the used spray powder and spray power, where the influence of spray powder is much higher than the influence of the spray power. The grain size range of the spray powder strongly influences the HAp content in the coating and the formation of CaO. The in vitro behavior of the coatings in simulated body fluid mainly depends on the contents of CaO and amorphous calcium phosphate, respectively. The formation of portlandite due to the reaction of the coating with the SBF is strongly influenced by the porosity of the coatings and can be used as an indicator for the depth of interaction between fluid and coating.

C. Hesse · M. Hengst · R. Kleeberg · J. Götze
Institute of Mineralogy, TU Bergakademie Freiberg,
Brennhausgasse 14, 09596 Freiberg, Germany

C. Hesse (✉)
Department of Mineralogy, Institute of Geology and Mineralogy,
Friedrich-Alexander-University Erlangen-Nuremberg,
Schlossgarten 5a, 91054 Erlangen, Germany
e-mail: hesse@geol.uni-erlangen.de

1 Introduction

Plasma-sprayed bioceramic coatings on bioinert substrates become very important for medical purposes such as thin films or thick coatings of prosthetic implants [1]. Because of its excellent biocombatibility and due to the similarity with bone material, hydroxyapatite [$Ca_{10}(PO_4)_6(OH)_2$, HAp] coatings on load-bearing substrates are commonly used in medical applications [2]. During the spraying process with its extremely high temperatures, the HAp powder undergoes changes in structure and chemistry. It is decomposed to α- and β-tricalcium phosphate [$Ca_3(PO_4)_2$, TCP], tetracalcium phosphate ($Ca_4P_2O_9$, TTCP), and lime (CaO) [3]. Additionally, HAp is transformed into oxyapatite [$Ca_{10}(PO_4)_6O$, OAp] [4]. Besides these crystalline phases, amorphous calcium phosphate (ACP) will be deposited on the substrate depending on the melting process of the HAp particles in the plasma. The amount of these phases in the coating depends directly on the spray conditions [5]. The phase composition of the coating was determined in different publications [3, 6] by scratching the complete coating from the substrate, milling the coating to a powder, and analyzing the powder by X-ray diffraction (XRD). Sun et al. [7] showed by XRD analysis of different coating layers that the composition and crystallinity of the coating varies between the coating surface and the substrate.

The solubility of the coating phases varies in a large range. CaO and the amorphous phase are dissolved easily in contact with simulated body fluid (SBF) [8, 9]. Thus, variations of the phase composition in the coating should also have an effect on the in-vitro behavior of the coating in SBF.

In this study, different highly crystalline HAp powders were used as feedstock for producing coatings on Ti6Al4V substrates. The phase composition of the coatings and their

variations with the coating buildup were investigated before and after incubation in SBF with regard to the spray power and the used feedstock.

2 Materials and methods

2.1 Feedstock and plasma-spraying

Three different feedstock powders with different grain size range were used for the experiments (Table 1). C90 is a very large grained powder whereas fHAp represents a very fine-grained powder. Both feedstocks are composed of spherical particles. The feedstock SM contains the widest grain size range and consists of fragments with cubic or rectangular shape. The powders of Sulzer Metco consist of highly crystalline pure hydroxyapatite with over 99 wt.% HAp. Analyses by XRD revealed that the used Captal 90 feedstock contains 98 wt.% HAp and 2 wt.% TTCP.

The powders were applied by atmospheric plasma-spraying (APS) [10] on Ti6Al4V substrates, sized $2 \times 5 \times 0.2$ cm^3. A PT-M1000 system (Plasmatechnik Wohlen, Switzerland) was used in conjunction with a F4 Plasmatron (Sulzer Metco). Table 2 summarizes the relevant experimental conditions. For each powder two coating series were produced with spray power of 30.3 and 22 kW. Coating thickness varies between different coatings. Coatings with fHAp feedstock contain the highest thickness of 380 μm.

2.2 Incubation experiments

One sample of each series was incubated in protein-free revised simulated body fluid (SBF) produced after Qyane et al. [11]. Each sample was stored in 300 ml SBF at a constant temperature of 37 °C for 8 weeks in a plastic box with the face upwards. The solution was not agitated. After this time, samples were dried at 100 °C for 24 h. Table 3 gives an overview about the samples.

2.3 Analytical methods

Coatings were gradually thinned under dry conditions in steps of 40 μm in minimum using abrasive paper (SiC). The abraded powder was used for infrared spectroscopy. Each prepared coating surface was analyzed by X-ray

Table 2 Plasma-spray parameters

Arc gas argon	45 l/min
Arc gas hydrogen	6.5 l/min
Arc current	399–400 A and 572–573 A
Arc voltage	53–55 V
Spray power	22 and 30.3 kW
Stand-off distance	90 mm
Transverse speed of plasma gun	100 mm/s

diffraction with a XRD 3000TT (Seiffert) with Cu K$_\alpha$ radiation. The operating voltage was 40 kV and the current 40 mA. The diffraction signal was detected over a range of 10° 2θ to 80° 2θ with a step wide of 0.03° and a measurement time of 5 s per step. The information depth of XRD is about 20 μm depending on porosity and mass absorption coefficient of the coating and therefore, a depth depending phase analysis was possible. Quantitative determination of phase composition was done by Rietveld refinement with the program BGMN. Structures used for refinement are given in Table 4. Cell parameters, microstrain, crystallite size, and the background were refined for each structure. Additionally, an amorphous phase was simulated automatically by a Lorentz function added to the refinement algorithm resulting in a better fitting of the background. The amorphous phase was located around 31° 2θ and 52° 2θ [12].

Evaluation of the crystallinity of the coatings was done after Tsui et al. [13] using the following equation:

$$\text{Crystallinity} (\%) = \frac{A_C}{A_C + A_A} \cdot 100\% \qquad (1)$$

where A_C is the total integrated intensity of the refined diffraction diagram of all crystalline phases in the range of 25–37° 2θ including HAp, TCP, TTCP, and lime. A_A is the integrated intensity of the calculated amorphous hump between 25 and 38° 2θ.

Additionally to the XRD analysis, Fourier transform infrared spectroscopy (FTIR) was done on the abraded powder if more than 1 mg powder was available. A FTS-40A spectrometer (BioRad, Germany) was used for recording the spectra. The powders were mixed with KBr in a weight ratio of $\sim$1:100 in an agate mortar and afterwards pressed into pellets. The spectra were recorded in transmission mode over a wave number range of 400–4000 cm^{-1}.

Table 1 Overview about used feedstock powders

Powder	Manufacturer	Grain size (μm)	Used abbreviation
Captal 90	Plasma Coating Limited, UK	100–140	C90
AMDRY 6021	Sulzer Metco	45–160	SM
XPT-D-701	Sulzer Metco	0–90	fHAp

Table 3 Overview about used samples and their description

Powder	Spray power 22 kW		Spray power 30.3 kW	
	As-sprayed	Incubated	As-sprayed	Incubated
Captal 90	C90_22 kW_assp	C90_22 kW_inc	C90_30 kW_assp	C90_30 kW_inc
AMDRY 6021	SM_22 kW_assp	SM_22 kW_inc	SM_30 kW_assp	SM_30 kW_inc
XPT-D-701	fHAp_22 kW_assp	fHAp_22 kW_inc	fHAp_30 kW_assp	fHAp_30 kW_inc

The sample name reflects the used feedstock and the spray power

Table 4 ICSD numbers of the used structures for Rietveld refinement

Phase	Lime	HAp	β-TCP	α-TCP	TTCP	Portlandite
ICSD-no.	75785	26205	6191	923	2631	15471

The surface roughness was analyzed by Mitutoyo Surftest SV 500 and the average of the roughness R_a was determined.

3 Results

3.1 Incubation experiments

The representative surface of the as-sprayed coatings is shown in Fig. 1a with sample C90_30 kW_assp. Cracks (arrow 1) and spherical particles (arrow 2) are typical for the surface. The incubation of the samples in SBF shows only small effects on the surfaces. Precipitates have been formed on all coatings with different amount. They are formed as thin but not closed layers (Fig. 1b) or as large precipitates with more then 500 µm in diameter (Fig. 1c). EDX analysis of the precipitations reveals a composition of HAp with a Ca/P ratio of 1.7.

3.2 Quantitative XRD analysis

Coatings prepared with Captal 90 contain the highest contents of hydroxyapatite of about 87 wt.% (C90_30 kW_assp) and 89 wt.% (C90_22 kW_assp), respectively, on the coating surface (Fig. 2). The bar chart of Fig. 2 shows a schematic cross-section of the coating and summarizes the phase distribution in dependence from the coating thickness. The width of the bars reflects the approximate information depth of the XRD analysis. Additionally, the calculated crystallinity is plotted in dependence from the coating thickness.

The coating thickness is 250 µm for sample C90_30 kW_assp and 150 µm for sample C90_22 kW_inc. R_a is about 10.8 ± 0.3 µm. The change of the hydroxyapatite content with increasing depth is very small. Near the substrate (∼40 µm thickness), the HAp content decreases to 81

(C90_30 kW_assp) and 85 wt.% (C90_22 kW_assp), respectively. With decreasing HAp content, the amounts of β-TCP and also of TTCP slightly increase. The crystallinity in Captal 90 coatings is about 90% at the surface in the as-sprayed coatings. Crystallinity decreases to 66% (C90_30 kW_assp) and 46% (C90_22 kW_inc), respectively, 20 µm above the substrate. The incubated samples show a decrease in crystallinity of about 4% at the surface after incubation. Within the coating, the crystallinity is comparable with the as-sprayed sample, but the loss of crystallinity near the substrate is less than in the as-sprayed samples. The content of CaO in the original samples 20 µm above the substrate is about 2.5 wt.%. After incubation in SBF no CaO was detected.

Coatings with the AMDRY-feedstock of Sulzer Metco are macroscopically equal to the C90 coatings but contain only 77 wt.% HAp on the coating surface. R_a is approximately 8.2 ± 1.5 µm. The coating thickness varies between 120 and 150 µm. The crystallinity at the surface is 81% in sample SM_30 kW_assp and 71% in sample SM_22 kW_assp. In both coatings, the TTCP content is about 15 wt.% at the surface (Fig. 3). The HAp content decreases from the surface to the substrate to 54 wt.% in sample SM_30 kW_assp and to 59 wt.% in sample SM_22 kW_assp. The CaO content of all SM samples is 2–3 wt.% on the surface. Samples sprayed with 30.3 kW contain 13 wt.% CaO 20 µm above the substrate. The CaO content in sample SM_22 kW_assp is about 10 wt.%. After incubation in SBF the CaO content near the substrate is reduced to 2 wt.% in sample SM_30 kW_assp and 1 wt.% in sample SM_22 kW_assp, respectively. Comparable with the C90 samples the loss of crystallinity on the surface is approximately 5% after incubation. The decrease of the HAp from surface to substrate is reduced by the incubation. Additionally, portlandite was detected below 100 µm coating thickness after incubation of sample SM_30 kW_inc.

Coatings of the fHAp feedstock have a higher thickness than the other coatings between 240 (fHAp_22 kW) and 380 µm (fHAp_30 kW). R_a is about 6.2 ± 1.5 µm. The HAp content of the coatings on the surface is about 45–50 wt.% which decreases to 22 wt.% at 20 µm above the substrate (Fig. 4). The CaO content is 10–12 wt.% on the surface and approximately 35 wt.% above the substrate. The coatings show a crystallinity of 54–91% on the surface. The
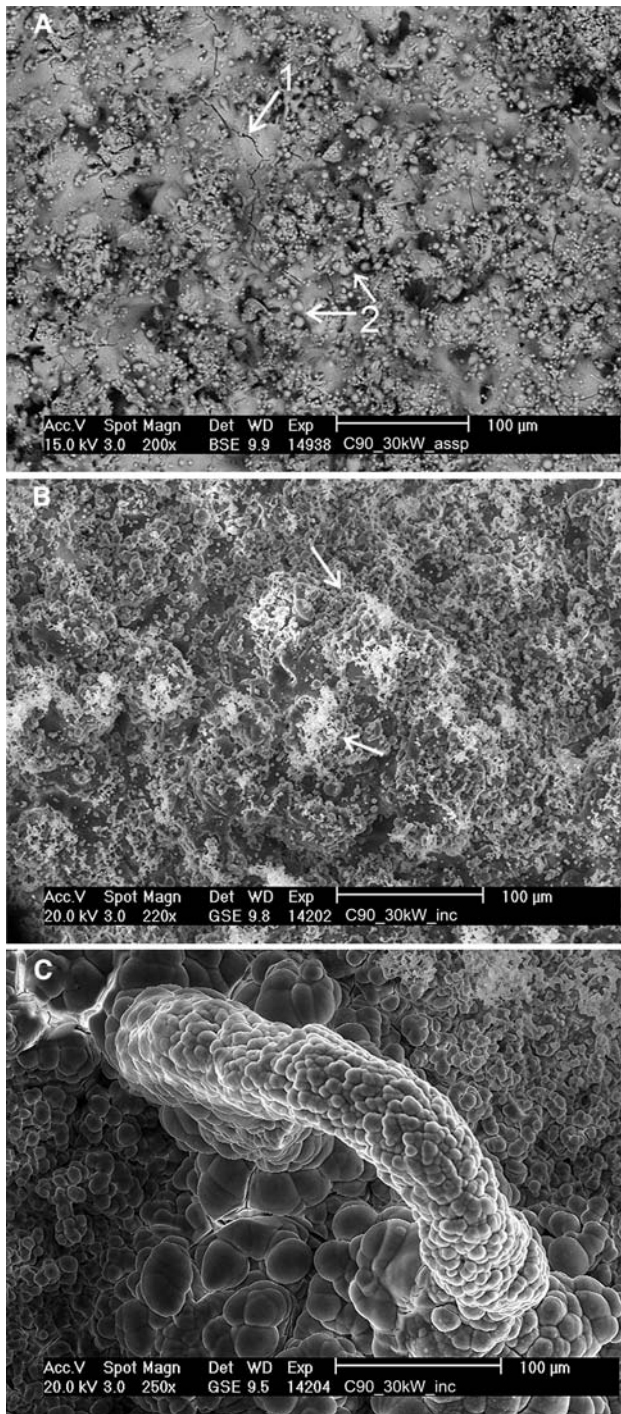
Fig. 1 ESEM images of the coating surface of samples C90_30 kW. (**a**) As-sprayed surface with cracks (arrow 1) and spherical particles (arrow 2), (**b**) incubated surface after 8 weeks with small precipitates (arrows), (**c**) incubated surface after 8 weeks with a large precipitate
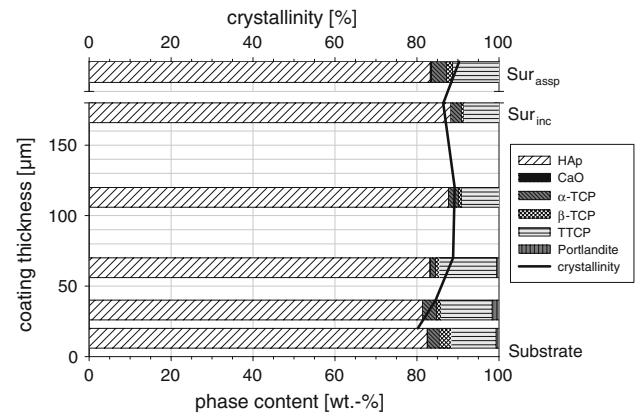

Fig. 2 Spatial variation of the phase composition of sample C90_30 kW_inc. Sur$_{assp}$, as-sprayed surface; Sur$_{inc}$, surface after incubation
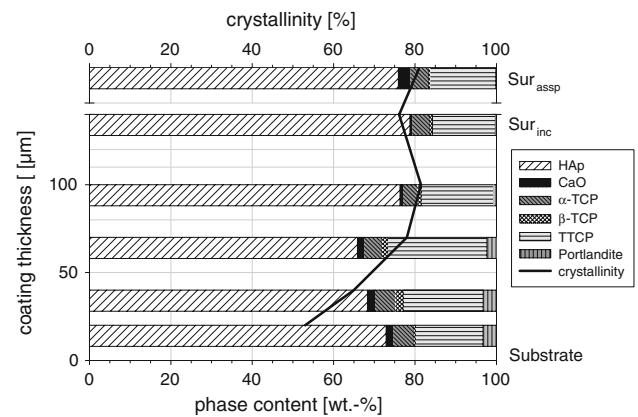

Fig. 3 Spatial variation of the phase composition of sample SM_30 kW_inc. Sur$_{assp}$, as-sprayed surface; Sur$_{inc}$, surface after incubation
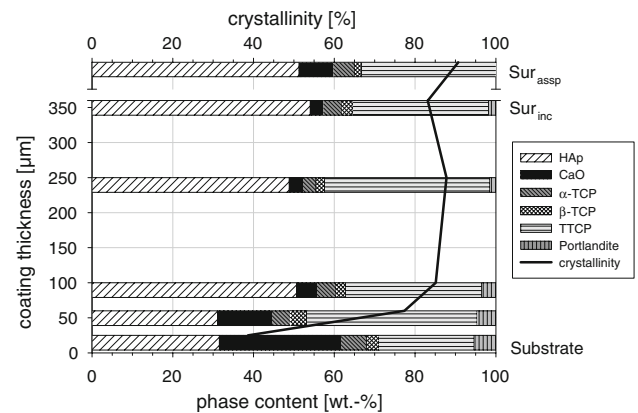

Fig. 4 Spatial variation of the phase composition of sample fHAp_30 kW_inc. Sur$_{assp}$, as-sprayed surface; Sur$_{inc}$, surface after incubation

variations of crystallinity between the samples are very high. Sample fHAp_22 kW_inc shows a crystallinity of 85% before incubation and sample fHAp_22 kW_assp only 54%. The high amorphous content reduces the quality of quantification and also the determination of crystallinity (Fig. 5).

The Lorentz function is only an approximation to the real amorphous hump, described by Gross et al. [14]. Therefore, quantities of the crystalline phase depend on the refinement of the amorphous phase. The coatings contain also a high
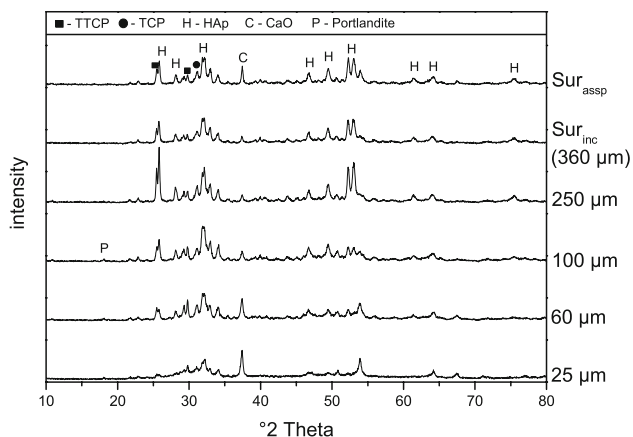
Fig. 5 XRD patterns of the incubated sample fHAp_30 kW_inc. The reflexes of the crystalline phases are shown in dependence on the coating thickness. The amorphous hump increases with decreasing coating thickness and decreasing intensity of the crystalline phases. Sur$_{assp}$, as-sprayed surface; Sur$_{inc}$, surface after incubation

amount of TTCP with approximately 30 wt.% (fHAp_30 kW_assp) and 22 wt.% (fHAp_22 kW_assp) on the surface. Portlandite occurs in the incubated samples in the complete coating from substrate up to the surface. The portlandite content is lower at the surface (1.5–2.0 wt.%) than close to the substrate (4–5 wt.%).

3.3 FTIR spectroscopy

FTIR spectroscopic analyses were performed on the feedstock and some powder samples produced during abrasion of the coatings.

Captal 90 shows all typical absorption bands for hydroxyapatite described by Fowler [15]. In sample SM, an absorption band of the v_2 doubly degenerated bending mode at 434 cm^{-1} is absent, and in fHAp the v_1 symmetric stretching mode at 962 cm^{-1} is lacking.
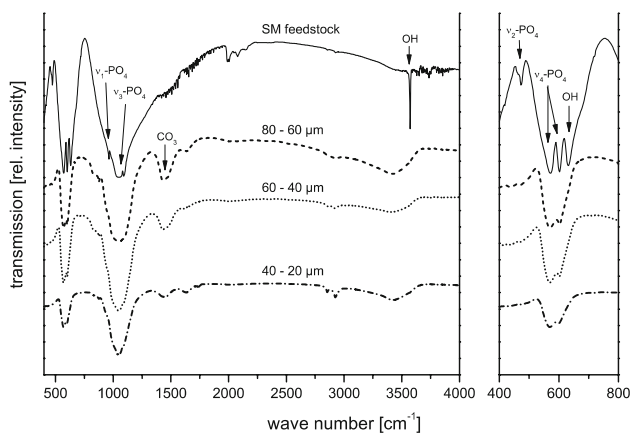

Fig. 6 IR spectra of the SM feedstock and selected abraded powders of the plasma-sprayed coating SM_22 kW_inc

Additional absorption bands at 875, 1445, 1535, and 1560 cm^{-1} appear in the FTIR spectra of all plasma-sprayed materials. The v_3 vibration modes of PO$_4$ between 1032 and 1087 cm^{-1} become smaller after the spraying process. The OH$^-$ stretching mode at 3572 cm^{-1} decreases or is missing in the samples (Fig. 6). Furthermore, the shape of the v_4 stretching modes of PO$_4$ has changed. The feedstock of SM shows two sharp absorption bands at 570 and 603 cm^{-1}. The intensity of these bands is reduced combined with a loss of sharpness after the spraying process.

4 Discussion

The comparison of the results of XRD and FTIR studies illustrates that the phase composition of the HAp powders underwent changes during the high temperature plasma-spray process. The content of HAp drastically decreases and some new phases were formed.

FTIR studies show the presence of additional absorption bands at 875, 1445, 1535, and 1560 cm^{-1}, which can be assigned to vibrations of carbonate apatite (CAp) [16]. The decrease of the intensities of the PO$_4$ v_4 stretching modes at 570 and 603 cm^{-1} is related to the loss of crystallinity during the spraying process, described by Sun et al. [7]. The reduction of the intensity of OH bending modes can probably be related to the dehydroxylation during the spraying process [7]. After Gross et al. [4], a shoulder on the 004 reflex of HAp between 52.2° 2θ and 54° 2θ in the diffraction pattern shows the presence of OAp. Unfortunately, this reflex is overlapped by peaks of TCP in the sample, so that the presence of OAp can only be predicted.

The XRD analysis shows a strong dependence of the phase composition of the coating on the used feedstock powder. Grain size and grain size range mainly influence the content of HAp in the coating. The spraying process of C90 shows a reduction of 10 wt.% to the feedstock HAp content. The melting of the particles is very low due to the small surface to volume ratio (SVR) of the particles. The degree of HAp decomposition increases with increasing SVR, resulting in a lower HAp content in the coatings (Fig. 7) and increasing contents of TTCP and CaO.

The spray power (SP) also influences the phase composition of the coatings. The HAp content at the surface of the C90 coatings is lower with higher SP, whereas the SM coatings do not show a dependency. The decomposition of C90 particles at higher SP is caused by the higher plasma temperature. In contrast, the HAp content at the surface of the fHAp coatings increases with a higher SP (30.3 kW). The duration time of the powder in the plasma is shorter resulting in a deposition of less decomposed particles at lower SP. The wide range in grain size of the SM powder causes the overlapping of properties of large and fine
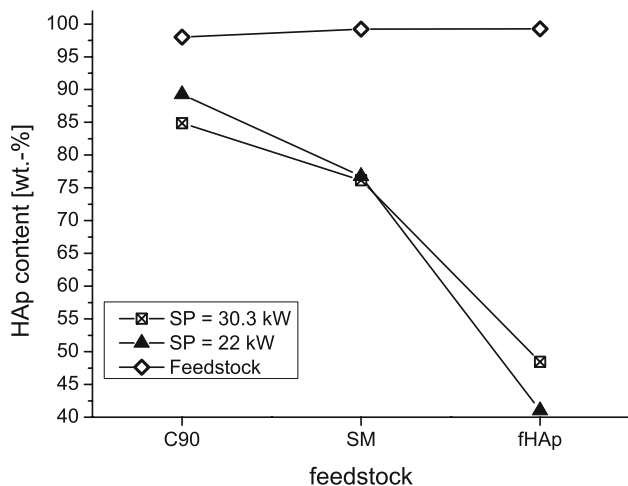
Fig. 7 HAp content in the spray powders and at the coating surfaces, respectively, in dependence on powder type and spray power (SP)

particles, and in consequence, no dependence of the HAp content on the spray power can be observed.

The crystallinity of phases within the coating also depends on the used feedstock and spray power, respectively. Higher SP causes higher crystallinity at the surface, and SM coatings show the lowest crystallinity (Fig. 8) similar to the coatings of series fHAp_22 kW.

The following incubation experiments in SBF further influence the crystallinity in the coatings. The crystallinity at the surface is lowered after the incubation period. ESEM images reveal spherical-shaped particles with a maximum diameter of 1 μm. Additional EDX analyses provide a Ca/P ratio of 1.5–1.61 for these precipitates. This ratio indicates the existence of Ca-deficient HAp according to studies of Götze et al. [17]. In XRD analysis the area of the amorphous hump increases after incubation accompanied by an
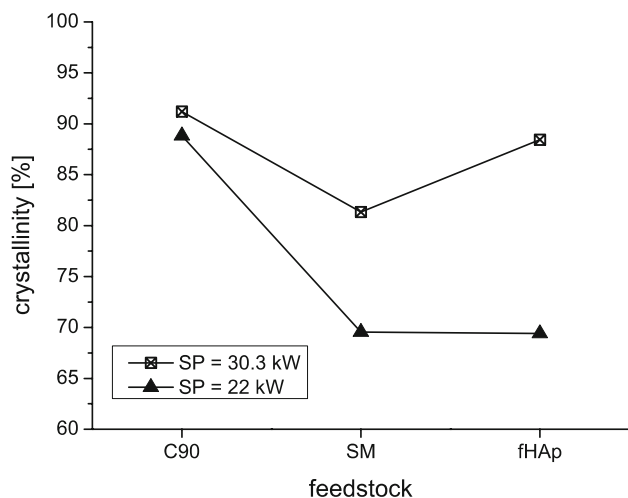
increase in HAp content. Therefore, the crystallite size of the formed precipitates is partly smaller than 10 nm. The so-called 'X-ray amorphous' crystalline matter could not be detected by XRD analysis [18]. The crystallinity within the coating is different for the as-sprayed and incubated sample. The decrease of crystallinity in the spatial profile from the surface to the substrate is smaller in the incubated coatings due to the degradation of ACP as the most soluble phase besides CaO (reviewed in [19]). The effect of ACP solution on the crystallinity is reduced by the contrary effect of formation of fine-scaled HAp aggregates.

The decomposition of HAp during the spraying process results in the formation of CaO. This phase was primarily found in coatings of fine-grained feedstock (SM and fHAp). Coatings of C90 also show a low content of CaO. Despite the high solubility of CaO, this phase was also found in the coatings after incubation in SBF. Furthermore, portlandite $[Ca(OH)_2]$ is formed during incubation. This phase is only stable at pH values >12.4. Hence, the occurrence of these two phases after incubation reflects the interaction between coating and SBF. The SBF penetrates the whole coating from the surface to the substrate, but the effective chemical reaction between coating and SBF depends on the coating porosity and is therefore only possible close to the surface. Due to the higher amorphous content and also the smaller particles in coatings produced by SM and fHAp, porosity in the coatings is very low and an interaction of the SBF with the coating is impaired. Therefore, the appearance of portlandite in the coating provides information about the porosity and the degree of degradation (Fig. 9).

Gu et al. [20] reported the dependence of CaO solution from the incubation duration. Therefore, an increase of the

Fig. 8 Crystallinity at the surface of the different as-sprayed coatings in dependence on the spray power (SP)
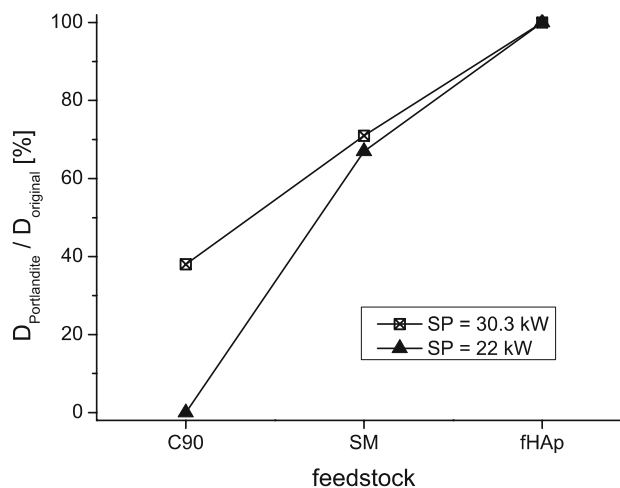

Fig. 9 Portlandite formation in the coating after incubation in SBF for 8 weeks in dependence on the spray power (SP). Values give the ratio (in %) between the coating thickness, where portlandite was determined below ($D_{Portlandite}$) and the as-sprayed coating thickness ($D_{original}$)

incubation period should result in a complete dissolution of CaO.

5 Conclusions

In the present study, HAp coatings were prepared on Ti6Al4V substrate by atmospheric plasma-spraying using different powders and varying experimental conditions, respectively. The spatial phase composition of these plasma-sprayed HAp coatings was investigated before and after incubation experiments in SBF. In general, the bulk plasma-sprayed hydroxyapatite coatings are composed of HAp, TTCP, α-TCP, β-TCP, CaO, and an amorphous phase. FTIR studies also showed a transformation of HAp to OAp and CAp during the spraying process.

The phase composition of the as-sprayed coatings, mainly the HAp content, varies with the used spraying feedstock. The coating is dominated by HAp using coarse-grained powder. Fine-grained HAp powder is decomposed during the spraying process and the resulting HAp content in the coating is very low. Increasing grain size of the used feedstock causes increasing crystallinity and porosity of the coating.

The investigation of separated 40 μm thick layers of the coatings enabled to provide information about the spatial phase distribution within the whole coatings. The results show that the phase composition varies within the coating buildup. Depending on the grain size and grain size range of the feedstock used, the HAp content is lowered down to 40 wt.% above the substrate.

Incubation experiments with the plasma-sprayed coatings in simulated body fluid illustrate the change of the phase composition. CaO and amorphous calcium phosphate are the phases which are in particular dissolved during the in-vitro experiments, whereas fine-grained HAp crystallizes at the coating surface. In addition, portlandite was formed in the coatings as an indicator for the interactions of the coating with the SBF. The occurrence and spatial distribution of that phase can also be correlated with the porosity of the coating, and therefore, is also an indicator for the biodegradability.

References

1. E. Wintermantel, S.-W. Ha, *Medizintechnik mit biokompatiblen Werkstoffen und Verfahren*. (Springer, Berlin, 2002)
2. K. De Groot, J. Ceram. Soc. Jpn. **99**, 917–926 (1991)
3. M.T. Carayon, J.L. Lacout, J. Solid State Chem. **172**, 339–350 (2003)
4. K.A. Gross, C.C. Berndt, P. Stephens, R. Dinnnebier, J. Mater. Sci. **33**, 3985–3991 (1998)
5. S.W.K. Kweh, K.A. Khor, P. Cheang, Biomaterials **23**, 775–785 (2002)
6. K.A. Gross, M.R. Phillips, J. Mater. Sci. Mater. Med. **9**, 797–802 (1998)
7. L. Sun, C.C. Berndt, C.P. Grey, Mater. Sci. Eng. **A360**, 70–84 (2003)
8. S.R. Radin, P. Ducheyne, J. Mater. Sci. Mater. Med. **3**, 33–42 (1992)
9. L. Sun, C.C. Berndt, K.A. Khor, H.N. Cheang, K.A. Gross, J. Biomed. Mater. Res. **62**, 228–236 (2002)
10. R.B. Heimann, *Plasma-spray Coating: Principles and Applications*. (VCH, Weinheim, 1996)
11. A. Oyane, H.-M. Furuya, T. Kim, T. Kokubo, J. Biomed. Mater. Res. Part A **65A**, 188–195 (2003)
12. W. Tong, Z. Yang, X. Zhang, A. Yang, J. Feng, Y. Cao. J. Chen, J. Biomed. Mater. Res. **40**, 407–416 (1998)
13. Y.C. Tsui, C. Doyle, T.W. Clyne, Biomaterials **19**, 2125–2029 (1998)
14. K.A. Gross, C.C. Berndt, H. Herman, J. Biomed. Mater. Res. **39**, 407–414 (1998)
15. B.O. Fowler, Inorg. Chem. **13**, 194–207 (1974)
16. J.C. Elliott, *Structure and Chemistry of the Apatites and Other Calcium Orthophosphates. Studies in Inorganic Chemistry*, vol. 18. (Elsevier, Amsterdam, 1994)
17. J. Götze, H. Hildebrandt, R.B. Heimann, Biomaterialien **2**, 54–60 (2001)
18. R.B. Heinmann, R. Wirth, Biomaterials **27**, 823–831 (2006)
19. L. Sun, C.C. Berndt, K.A. Gross, A. Kucuk, J. Biomed. Mater. Res. **58**, 570–592 (2001)
20. Y.W. Gu, K.A. Khor, P. Cheang, Biomaterials **24**, 1603–1611 (2003)